Comparison of the Tornadic and Nontornadic Supercells Intercepted by VORTEX2 on 10 June 2010

ALICIA KLEES*, YVETTE RICHARDSON, AND PAUL MARKOWSKI

Penn State University, University Park, PA

1. Introduction

Determining which particular supercell thunderstorm will generate tornadoes is a serious challenge; both nontornadic and tornadic supercells alike can have significant low-level rotation on the mesocyclone scale (Markowski et al. 2011), and the majority of supercells never produce tornadoes. Increasing our understanding of the differences in internal processes and characteristics of nontornadic and tornadic supercells is crucial, as it could lead to more accurate forecasting of tornadogenesis, increased warning accuracy, and a decreased number of false alarms, potentially saving lives and property.

The second Verification of the Origins of Rotation in Tornadoes Experiment (VORTEX2) was designed to study such processes and characteristics by collecting wind (radar) and thermodynamic (sounding, mobile mesonet, and StickNet) observations within tornadic and nontornadic supercells (Wurman et al. 2012). This study focuses on the rare set of observations collected by VORTEX2 on a pair of supercells, one tornadic and the other nontornadic, evolving in close proximity to each other in northeastern Colorado on 10 June 2010.

On this day, an approaching upper-level shortwave trough induced lee cyclogenesis in southeastern CO. The synoptic-scale features on 10 June, combined with the terrain, generated an environment in northeastern Colorado that was favorable for the development of severe weather. By 2230 UTC, a pair of supercells initiated approximately 50 km apart from each other, just to the east of the foothills of the Rocky Mountains in northeastern Colorado.

VORTEX2 intercepted the northern of these two supercells from 2345–0040 UTC, and then, VORTEX2 deployed on the more impressive supercell to the south from 0100–0230 UTC. This southern storm generated two tornadoes from 0109–0115 UTC and 0122–0126 UTC, respectively.

This case provides a valuable opportunity to study rare, detailed observations of nontornadic and tornadic supercells occurring in close proximity. We examine differences in the outflow characteristics, environments, and interactions with others storms in order to develop a hypothesis for why tornadogenesis failed in the first supercell and succeeded twice in the second supercell. We also study, for the second storm, the two tornado events and the subsequent evolution of the mesocyclone.

2. Data and methods

The VORTEX2 armada collected an extensive data set on 10 June 2010. Radar data used in this study were collected by the SMART-Radar 1 (SR1) and SMART-Radar 2 (SR2) (Biggerstaff et al. 2005), NOXP, and DOW7 (Wurman et al. 1997) radars (Fig. 1). Radar data were first edited using the National Center for Atmospheric Research (NCAR) Solo II radar data editing and visualization software (Oye et al. 1995). Edited radar data were objectively analyzed to a Cartesian grid using the two-pass Barnes successive corrections method (Barnes 1964; Koch et al. 1983; Majcen et al. 2008). Dual-Doppler syntheses were completed by applying an upward integration of the anelastic mass continuity equation to the radar velocity data, with iterative adjustments made to the fields (Brandes 1977; Dowell and Shapiro 2003). For both storms, dual-Doppler syntheses were completed using SR1 and SR2 radar data.

Other data used in this case study include sounding and mobile mesonet data. Twenty-one MGAUS radiosondes were launched on 10 June to collect sounding profiles. For each sounding, numerous environmental parameters were calculated and analyzed, with focus on the soundings with the closest spatial and temporal proximity to each of the storms. Six Penn State-NSSL mobile mesonet vehicles with mounted instruments (Straka et al. 1996; Waugh and Fredrickson 2010) collected near-surface thermodynamic and wind data in the outflows of both supercells. Time-to-space converted, smoothed data were used to evaluate the virtual and equivalent potential temperature deficits across the outflows of both supercells.

───────────

Corresponding author address: Department of Meteorology, Penn State University, 503 Walker Building, University Park, Pennsylvania. E-mail: amk5375@psu.edu
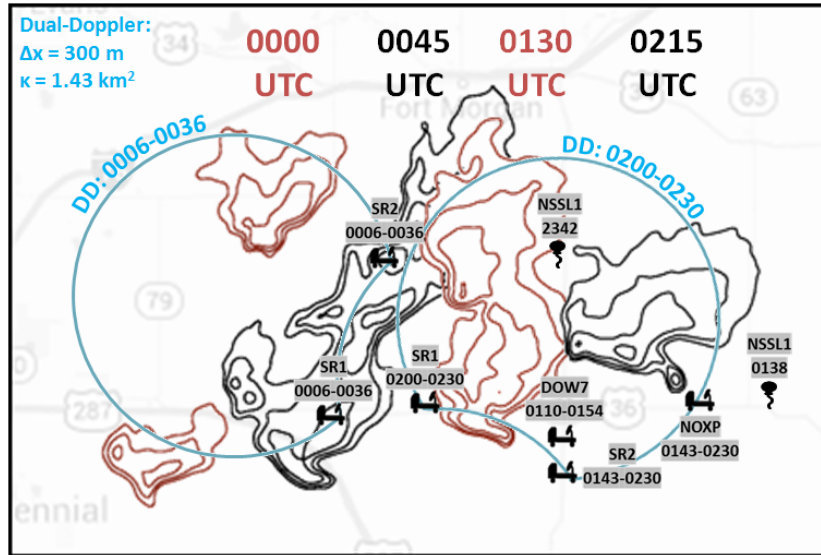
FIG. 1: Deployment map for 10 June 2010. Reflectivity contours are shown every 45 minutes for the nontornadic (northern) and tornadic (southern) supercells. Radar truck icons show the location of each mobile radar deployment, with time ranges (UTC) in grey boxes. Balloons denote the location of example mobile sounding launches, with launch time (UTC) in grey boxes. Dual-Doppler lobes are in blue, with dual-Doppler time periods noted. VORTEX2 deployed on the nontornadic supercell first (0006–0036 UTC) and then the tornadic supercell (0110–0230 UTC).
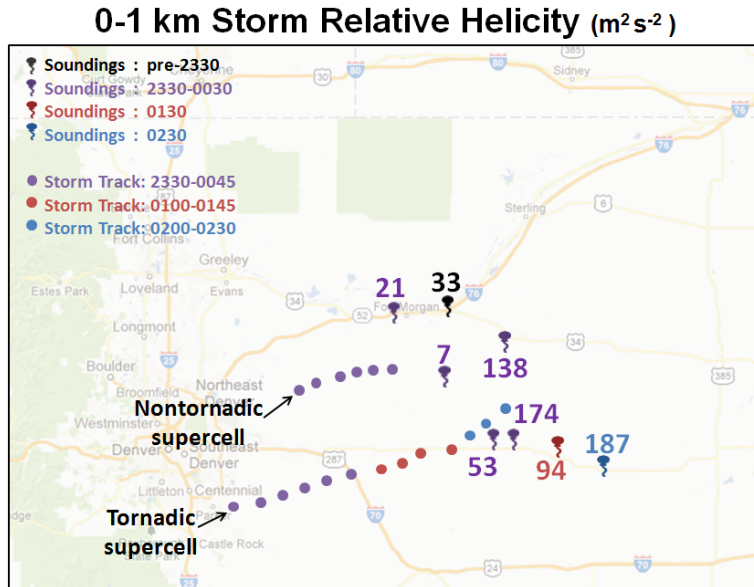

FIG. 2: 10 June 2010 storm environment as represented by 0–1 km storm-relative helicity (m^2 s^{-2}). Balloon icons denote the launch location of each sounding, color-coded with respect to launch time. Dots denote the storm tracks, based on the location of the midlevel mesocyclone, and are color-coded with respect to time.

3. Results

a. Storm environments

Values of all thermodynamic and most kinematic environmental parameters were not significantly different between the environments of the two supercells. Both environments had moderate CAPE, marginal 0-6 km vertical wind shear (typically below 40 knots), and LCLs around 1200–1300 m.

Values of 0–1 km storm-relative helicity (SRH1) were somewhat higher in the environment of the tornadic su-
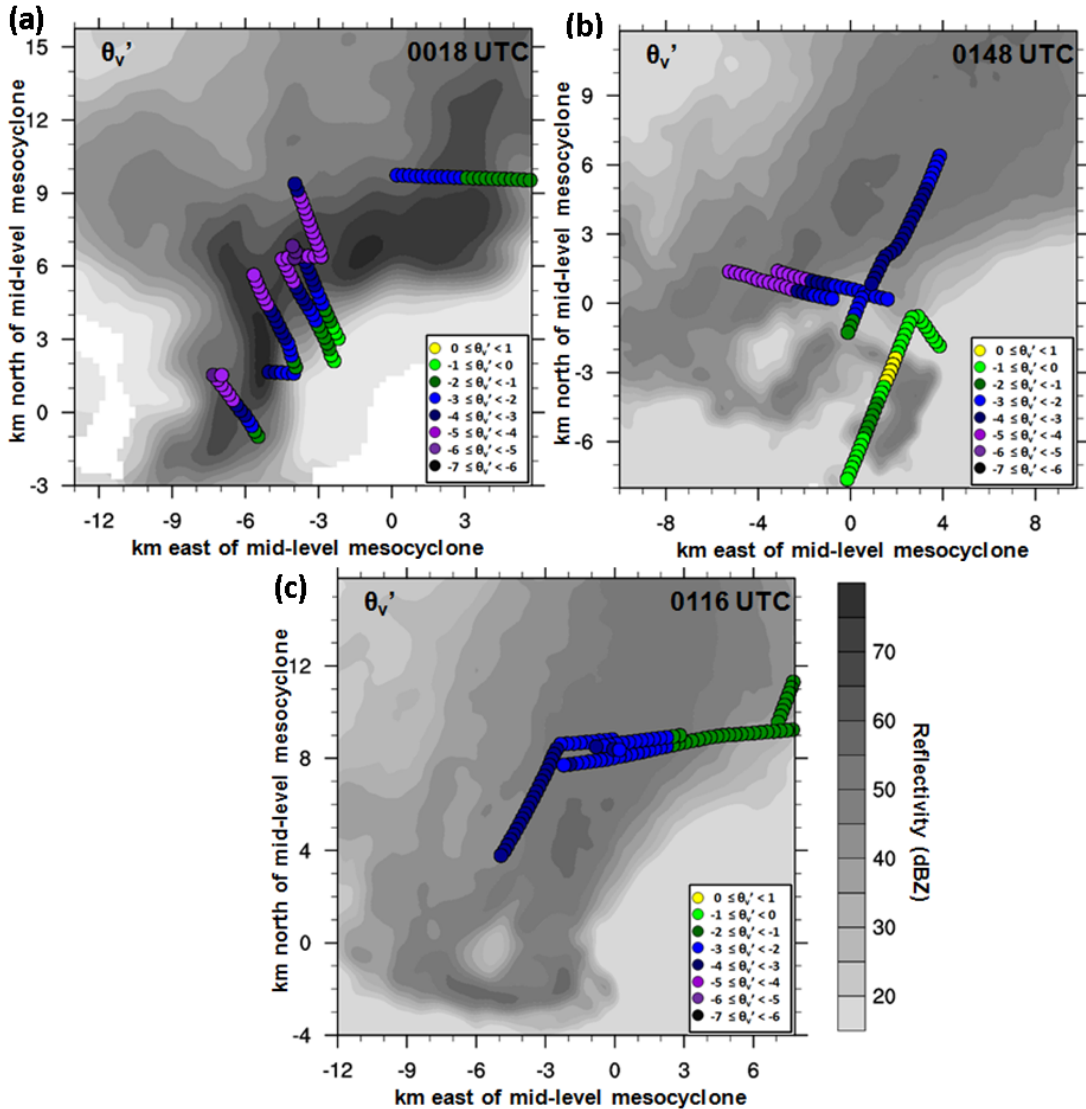
FIG. 3: Mobile mesonet-measured virtual potential temperature perturbations (color-coded circles) in the outflow of (a) the nontornadic supercell at 0018 UTC (base state: 315.9 K), (b) the tornadic supercell at 0148 UTC (base state: 314.7 K) and (c) the tornadic supercell at 0116 UTC (base state: 314.7 K). Temperature perturbations are overlayed on logarithmic equivalent reflectivity factor from SR2 (750 m), NOXP (800 m), and DOW7 (800 m), respectively.

percell (53–187 m^2 s^{-2}) than that of the nontornadic supercell (7–138 m^2 s^{-2}) (Fig. 2), suggesting that the environment of the tornadic supercell was slightly more favorable for tornado generation. However, SRH1 in both environments, while within climatology for weakly tornadic supercells, was marginal with respect to significantly tornadic supercells.

b. Outflow characteristics

Measurements collected by the mobile mesonet fleet suggest that neither storm on 10 June 2010 had particularly large virtual potential temperature deficits across the outflows, with maxima rarely exceeding 5–6°C at any time. For example, at 0018 UTC, a θ_v deficit of 5°C was measured across the nontornadic supercell's RFD, which falls within the typical range of θ_v deficits in nontornadic/weakly tornadic supercells of 4–7°C (Markowski et al. 2002) (Fig. 3a). During the tornadic supercell's nontornadic phase, at 0148 UTC, a θ_v deficit of 5°C was also observed in a similar region (Fig. 3b). During the tornadic supercell's tornadic phase, unfortunately there were only measurements available in the northern flank of the storm owing to a sparse road network and ongoing re-
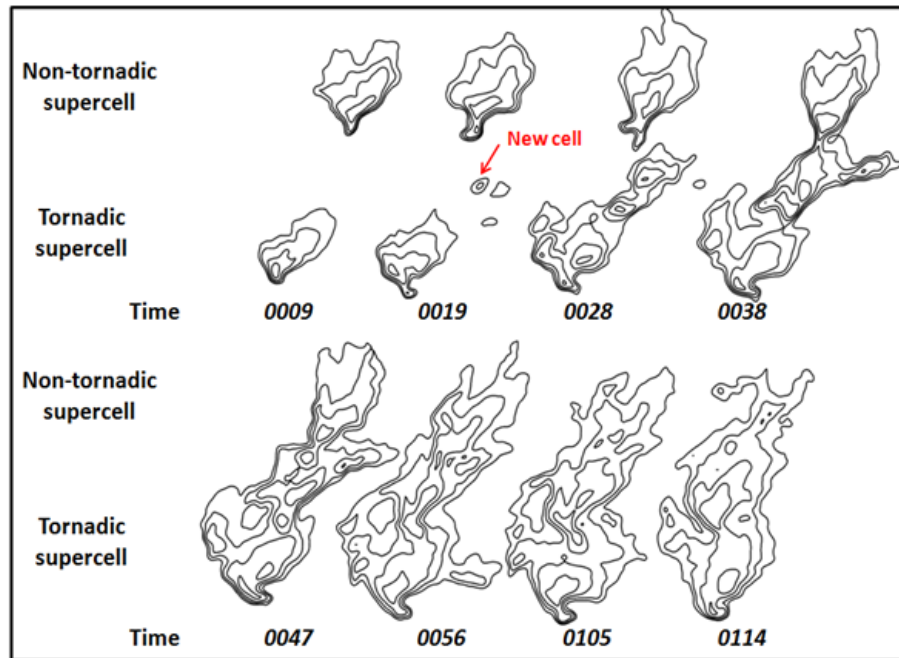
FIG. 4: Progression of interactions between original cells and the new cell (pointed out in red). Contours are of KFTG-88D logarithmic equivalent reflectivity factor, every 10 dBZ beginning at 25 dBZ, at heights of 1.5 km (0009–0047 UTC) or 2.0 km (0056–0114 UTC).

deployment. However, where data were available, the maximum θ_v deficit was 4°C, not much warmer than θ_v deficits in the nontornadic supercell (Fig. 3c).

At most times in both storms, outflow temperatures were consistent with storms that produce weak tornadoes. Both outflows were, however, cold relative to typical outflows in significantly tornadic supercells.

While the environments and outflow characteristics of the two supercells were, for the most part, comparable, the two storms had different interactions with other convection.

c. Cell interactions

Both supercells interacted with a new storm that developed between them. The merger of the nontornadic supercell with this cell ultimately led to the nontornadic supercell's demise. On the other hand, the tornadic supercell's interaction with this new storm may have made tornadogenesis more favorable.

By 0014 UTC, this new cell, hereafter referred to as Cell A, initiated between the nontornadic and tornadic supercells, near the intersection of their gust fronts (Fig. 4). Over time, Cell A intensified, increased in size, and began merging with the nontornadic supercell (Fig. 4). The nontornadic supercell seemed to experience detrimental impacts from the merger event from 0027 UTC onward.

Dual-Doppler analyses suggest that the updraft and mesocyclone in the nontornadic supercell generally weakened beginning at 0027 UTC. Updraft mass flux decreased from 0027 UTC onward, indicating a weakening of the updraft (Fig. 5). Similarly, analyses of mesocyclone strength, measured in terms of circulation (at a radius of 1 km), show that the strength of the mesocyclone decreased quite significantly from 0024/0027–0033 UTC, dropping by at least 20000 m^2s^{-1} over this time period at various heights (Fig. 5).

The merger weakened the updraft and the mesocyclone through a combination of (1) cooling the inflow and (2) raining into the updraft. First, the maximum θ_v deficit in the inflow region at 0051 UTC (during the peak of the merger) was up to 4°C colder than θ_v deficits measured in this region at 0012 UTC (well-prior to the merger) (Fig. 6), and equivalent potential temperature deficits, up to 2°C colder. These differences indicate that the inflow was a few degrees colder after the merger.

Second, as Cell A approached and then merged with the supercell, the updraft became increasingly ensconced in reflectivity. Quantitatively, the percentage of points in the updraft having reflectivity values exceeding 35 dBZ jumped from just above 10% to over 90% between 0024 UTC and 0033 UTC (Fig. 7).

As the mesocyclone and updraft weakened for the aforementioned reasons, the storm increasingly lost its supercellular structure and was ultimately consumed by Cell A.
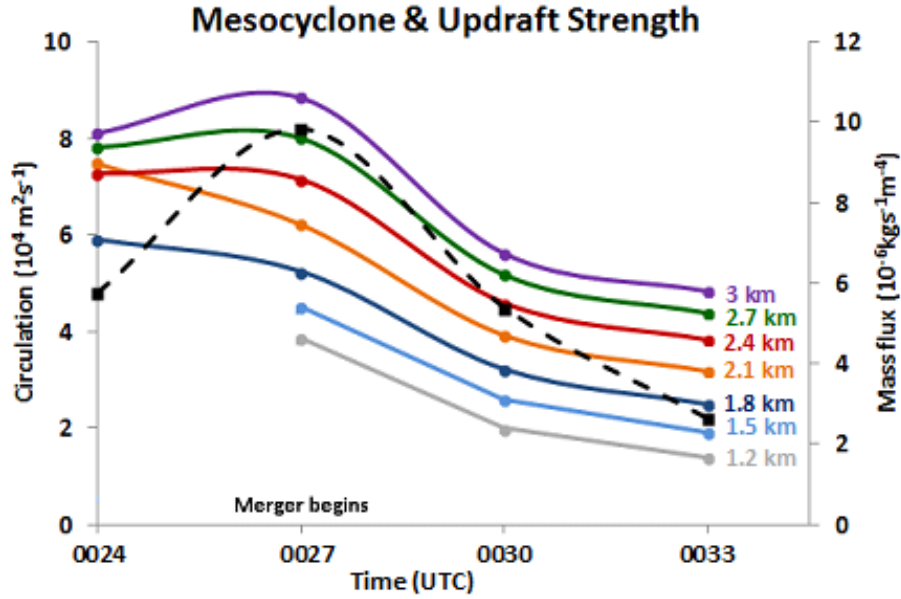
FIG. 5: Impacts of merger on characteristics of the nontornadic supercell, in terms of the time evolution of updraft strength (mass flux, dashed black curve; $10^{-6}\mathrm{kgs}^{-1}\mathrm{m}^{-4}$) and mesocyclone strength (maximum circulation at a radius of 1 km, colored solid curves; $10^4\mathrm{m}^2\mathrm{s}^{-1}$)
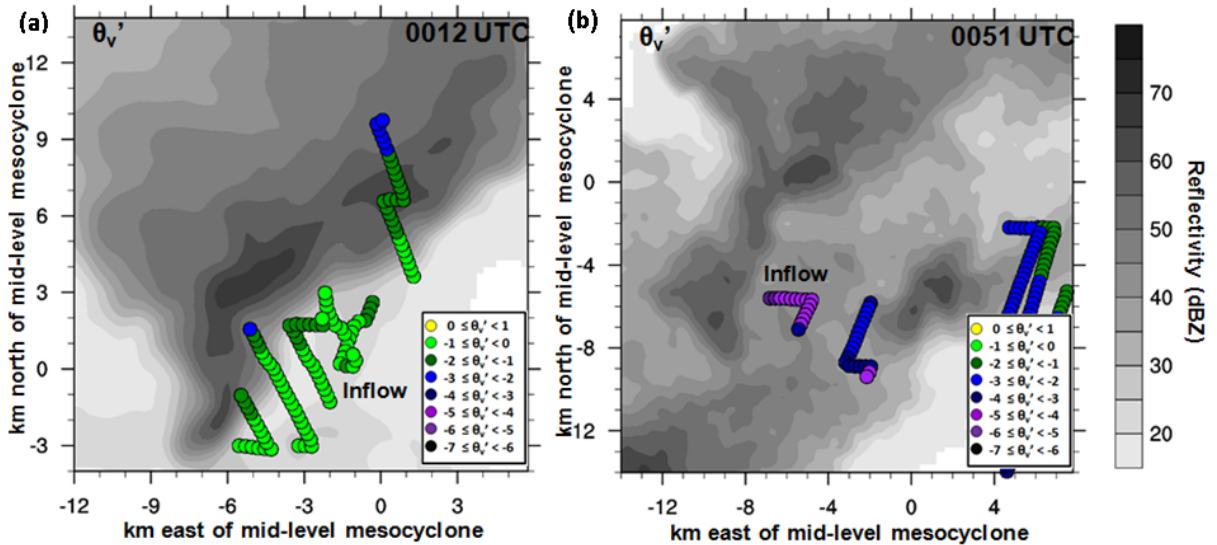

FIG. 6: Mobile-mesonet measured virtual potential temperature perturbations (color-coded circles, relative to base state of 315.9 K) in the inflow region of the nontornadic supercell at (a) 0012 UTC, overlayed on 750 m SR2 logarithmic equivalent reflectivity factor (dBZ, shaded contours) and (b) 0051 UTC, overlayed on 1.2 km KFTG 88D logarithmic equivalent reflectivity factor (dBZ, shaded contours).

While Cell A was detrimentally merging with the non-tornadic supercell, it was also interacting with the northern flank of the tornadic supercell. This interaction may have made tornadogenesis more favorable in this supercell than it otherwise would have been. Refer to 'Future Work' for further elaboration on this possibility.

d. Tornado evolution

While the nontornadic supercell was gradually dying, the tornadic supercell generated two (visible) tornadoes (Fig. 8). The first tornado developed at approximately 0109 UTC and had a visually well-defined funnel, as it was located to the east of the bulk of the precipitation. It
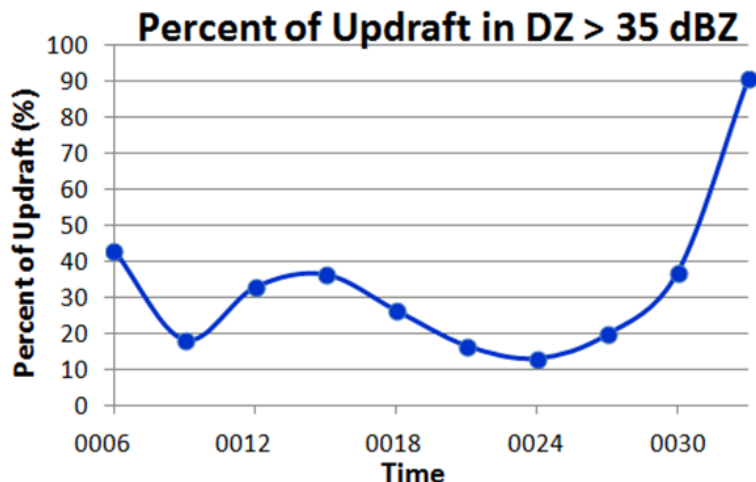
FIG. 7: Percent of the updraft in reflectivity of at least 35 dBZ at 2.5 km.

tracked to the east and maintained a constant strength, at or above tornado strength (40 m s^{-1}), at all heights analyzed until 0114 UTC (Fig. 9). Then, at almost all heights, the radial velocity differential weakened by at least 5 m s^{-1}, even falling below tornado strength aloft (Fig. 9). Correspondingly, visual ground observations indicate that the condensation funnel lost contact with the surface a little after 0115 UTC.

For the next approximately 7 minutes, there was no visible condensation funnel present. During this transition time, the circulation aloft (1 to 2.5 km) generally maintained at least tornado strength (Fig. 9). However, closer to the surface, around 0.5 km, the circulation had weakened by 0116 UTC, and still had a decreased strength (below tornado strength) past 0118 UTC. Certainly, something went awry in these lower levels to result in the lack of a visible funnel, but the cause of this cannot be evaluated, as there is no dual-Doppler data available.

The second tornado began at approximately 0122 UTC. The strength of the circulation weakened at all heights throughout the tornado's short life, especially from 0124–0126 UTC. During these last two minutes of the tornado's life, the radial velocity differential was typically below tornado strength, even dipping as low as $20–25 \text{ m s}^{-1}$ by 0126 UTC (Fig. 9). Throughout its lifetime, the second tornado was rain-wrapped, likely due to an amplification of a surge in the rear-flank downdraft region to its south that resulted in the tornado experiencing westward storm-relative motion.

The evolution of the 10 June 2010 tornadoes did not follow the classic model of cyclic mesocyclogenesis prior to the production of a new tornado (Burgess et al. 1982). Rather, the same mesocyclone that produced the first tornado generated the second tornado minutes later. The pro-cess causing the spin-up of the second tornado cannot be evaluated with the single-Doppler data.

e. Mesocyclone evolution

After the two tornadoes, the supercell entered a long nontornadic phase. During this time, the mesocyclone underwent an interesting cyclic evolution. At least two new cyclonic circulations [defined per French et al. (2008)] were observed to develop in the rear-flank region of the storm and move rearward relative to the rest of the storm, consistent with the behavior of such circulations in previous studies (French et al. 2008; Dowell and Bluestein 2002). In contrast, an anticyclonic circulation remained firmly anchored in place during this time period.

The first cyclonic circulation tracked, 'C1,' consisted of the remaining circulation from the second tornado. By 0131 UTC, C1 had moved backward in the RFD (Fig. 10a,b) and then continued its rearward motion. By 0147 UTC, 'C2' formed in the reflectivity hook and began traveling rearward in the storm (Fig. 10c). As time progressed, an anticyclonic circulation, 'A1,' began significantly strengthening. A1 had been present, albeit weaker, from prior to 0131 UTC. It is noteworthy that for much of the subsequent time analyzed, A1 was of comparable or greater strength than the cyclonic circulations present (based on radial velocity differential).

By 0204 UTC, a new circulation, 'C3,' was rapidly developing well to the east-northeast of C2 and northwest of the anticyclonic vortex, along the rear-flank gust front (Fig. 10f). Like C1 and C2, over time, C3 moved rearward relative to the rest of the storm (Fig. 10g-j). Throughout this cycling, A1 experienced very little storm-relative motion. Analyses of storm-relative streamlines show that A1 was in virtually zero storm-relative flow, whereas the cyclonic circulations were embedded in strong midlevel rearward storm-relative flow.
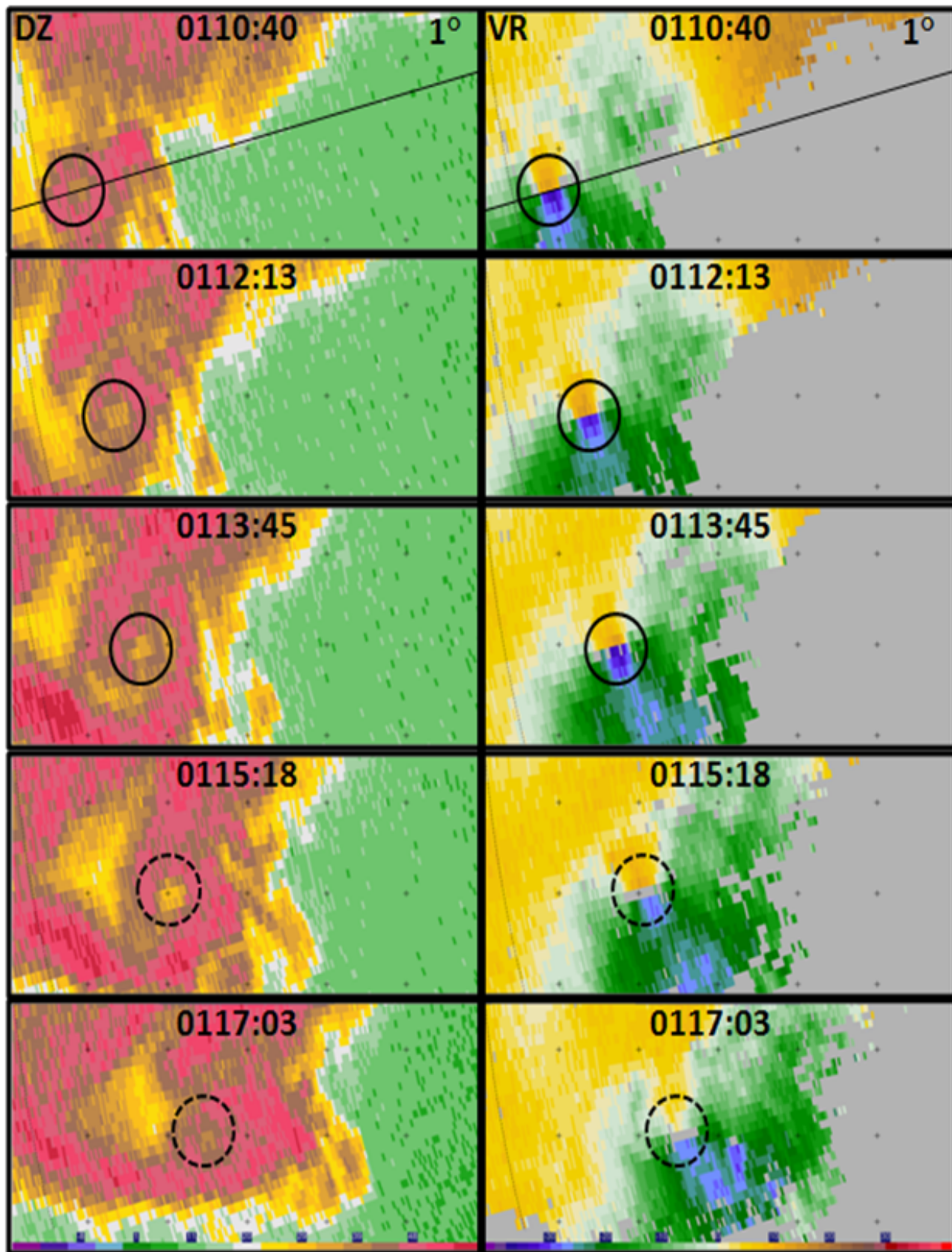
FIG. 8: Evolution of both tornadoes (and transition period in-between), shown by logarithmic equivalent reflectivity factor (left; dBZ) and velocity (right; m s^{-1}) data from 400–500 m AGL DOW7 sweeps. Circles indicate the location of the radial velocity couplet at each time. Solid (dashed) circles are used if a tornado is present (is not present). Tick marks are spaced every 2 km. DOW7 is 30 km from the first tornado at 0110:40, and only 15 km from the second tornado at 0126:09.
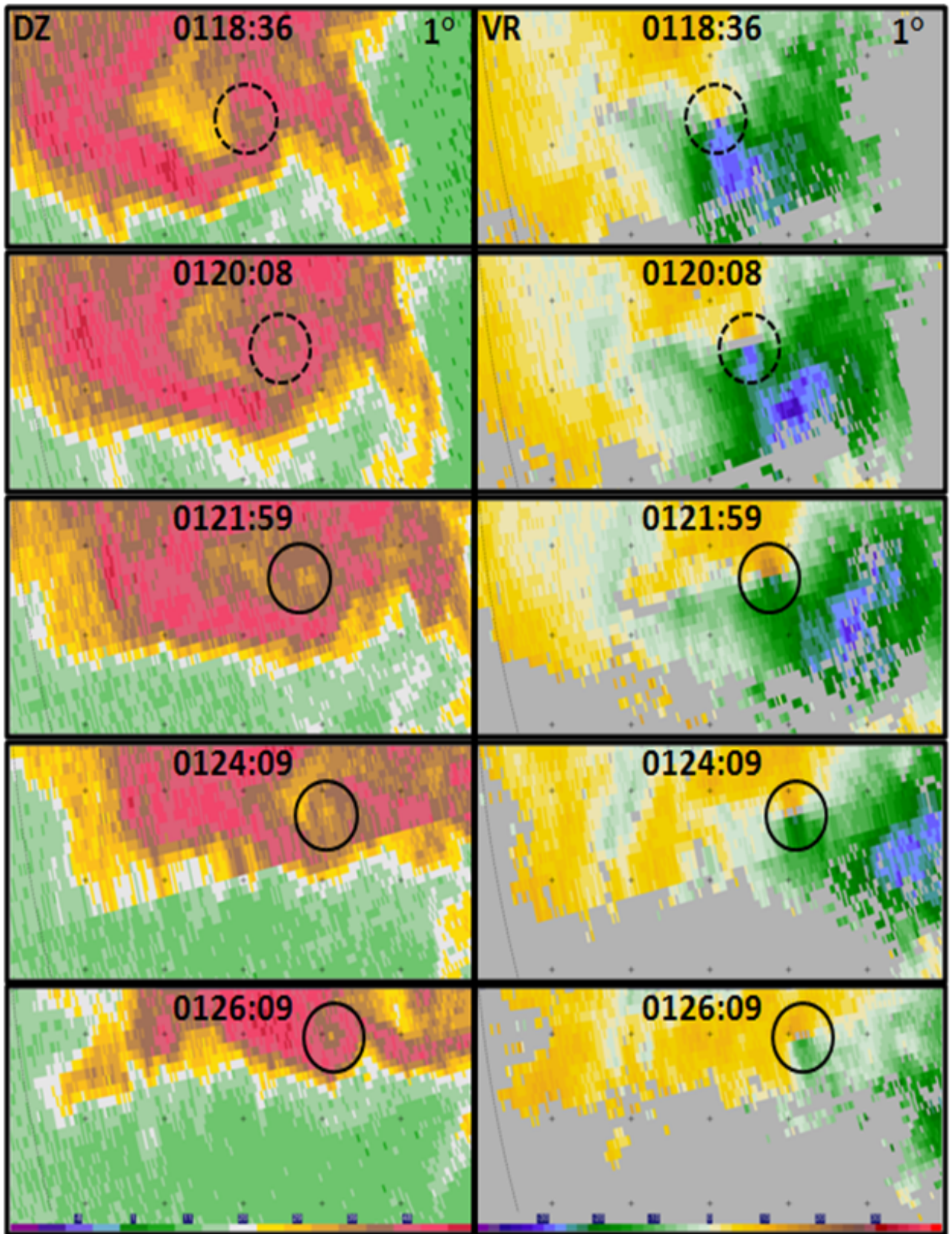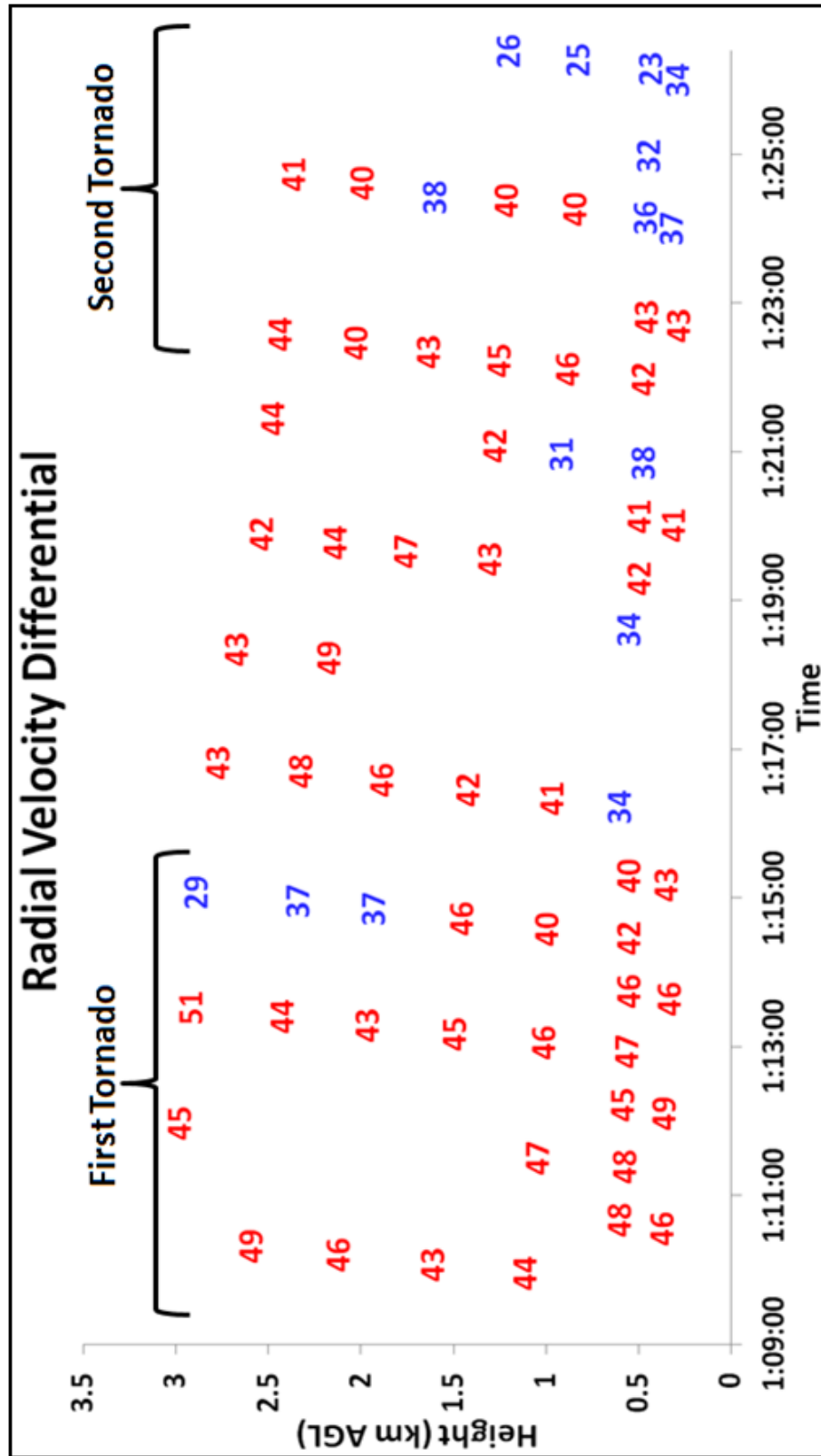
FIG. 8: continued

FIG. 9: Radial velocity differential (m s^{-1}; red if greater than tornado threshold of 40 m s^{-1}, blue if less than 40 m s^{-1}) calculated using gate-to-gate (or one gate separation due to noise in the data) radial velocity data from the raw 0.5°, 1°, 2°, 3°, 4°, 5°, and 6° DOW7 sweeps during the first tornado (0109–0115 UTC), transition period in-between (0115-0122 UTC), and the second tornado (0122–0126 UTC).
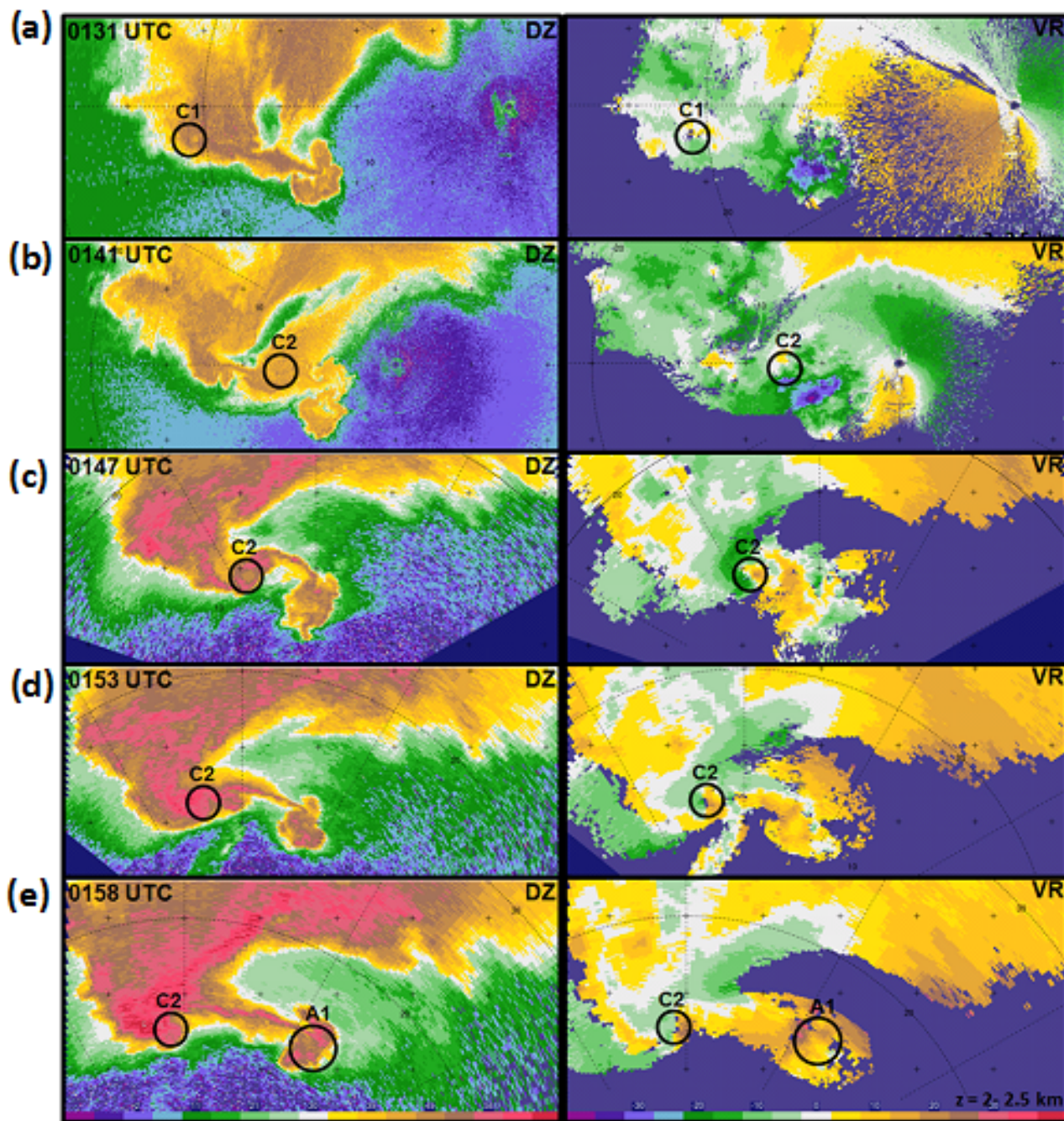
FIG. 10: Radar logarithmic equivalent reflectivity factor (left, dBZ) and radial velocity (right, m s^{-1}) at approximately 2-2.5 km (depending on location of particular circulation) from DOW7 [(a) and (b)] and SR2 [(c)-(j)] at the times noted (approximately every 6 minutes). Labeled black circles show cyclonic and anticyclonic circulations. Note that DOW7 reflectivity [(a) and (b)] is uncorrected.
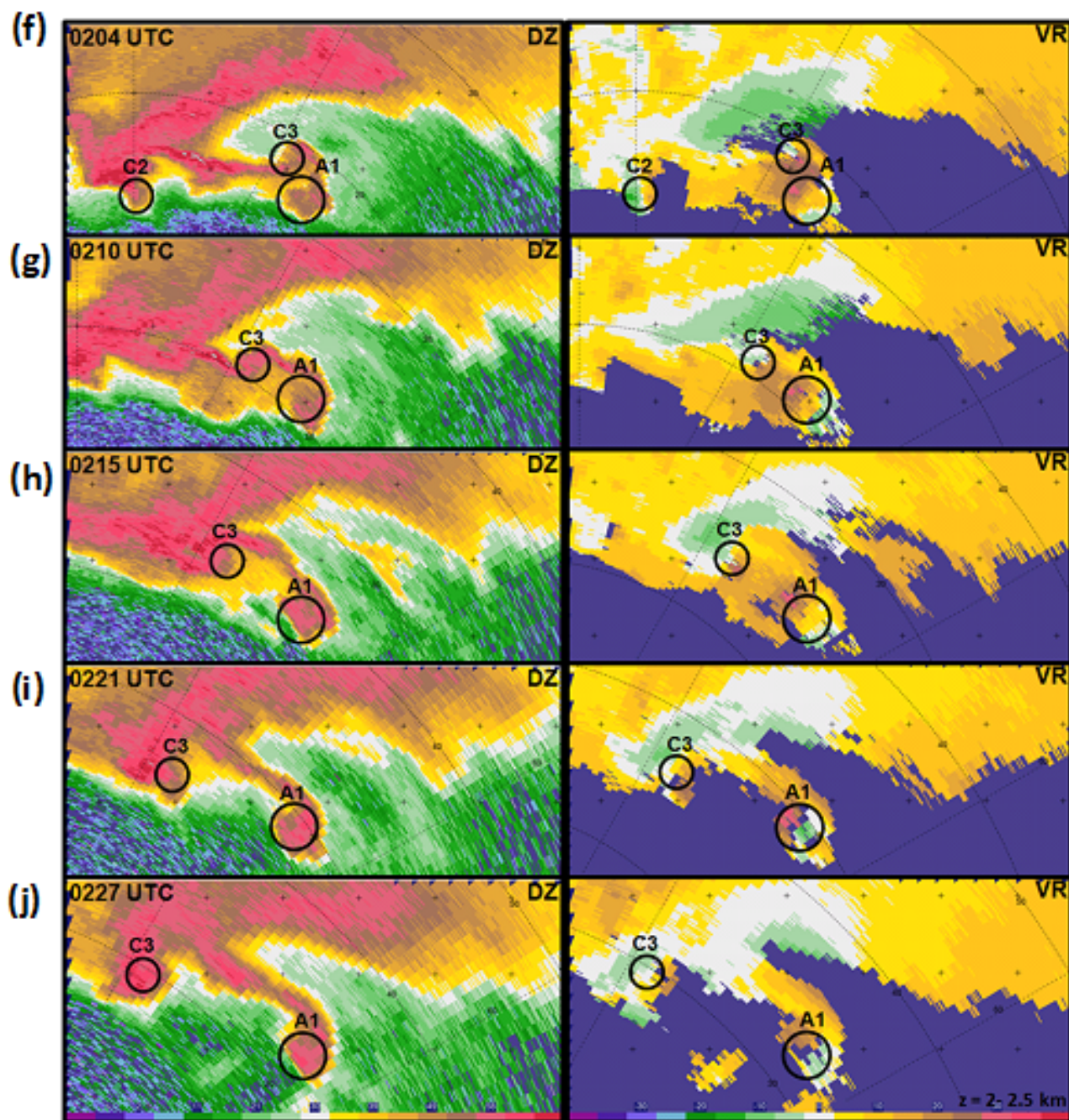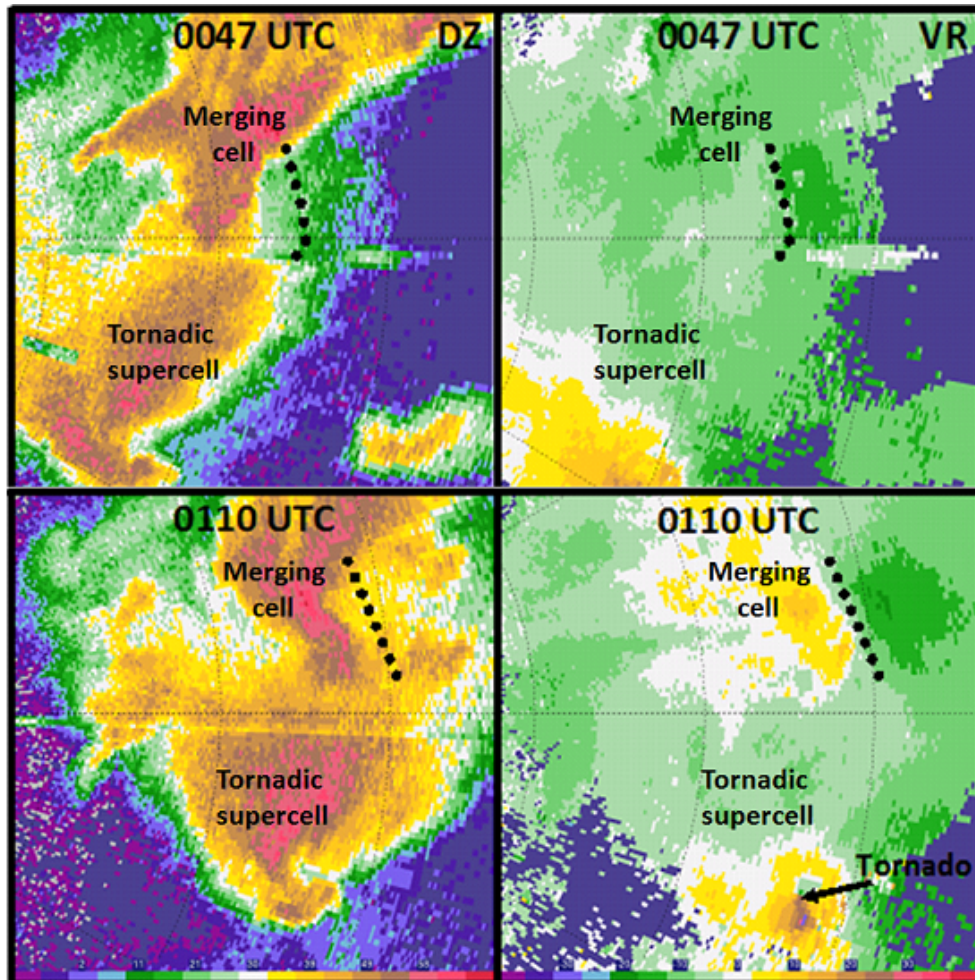
FIG. 10: continued

FIG. 11: KFTG-88D logarithmic equivalent reflectivity factor (left; dBZ) and radial velocity (right; m s^{-1}) at (a) 0047 UTC and (b) 0110 UTC. Dotted line denotes the gust front associated with the outflow of Cell A. Tornado is denoted in (b).

4. Summary and conclusions

In this study, we analyzed a nontornadic and a tornadic supercell intercepted by VORTEX2 on 10 June 2010, and compared the storm environments, outflow strengths, and interactions with other convective features. The goal was to identify differences and use these to hypothesize why one supercell never produced a tornado and the other produced at least two. Additionally, for the tornadic supercell, the evolution of the two tornadoes and the mesocyclone were studied.

Both storms developed in environments that were fairly similar and, for the most part, somewhat marginal for the development of tornadoes (especially significant tornadoes). The main difference was more low-level storm-relative helicity in the environment of the tornadic supercell. The storms had outflows with similar thermodynamic characteristics (at locations/times at which there were data); the outflows were cold relative to those typical of supercells producing (significant) tornadoes.

The most important difference between the two supercells appeared to be how each interacted with Cell A, the storm which initiated between them. The nontornadic supercell merged with Cell A, and this merger led to the demise of the nontornadic supercell by weakening the updraft and mesocyclone through a combination of raining into the updraft and cooling the inflow of the supercell. Had this merger not happened, would this supercell have been able to produce a tornado? It took the tornadic supercell nearly three hours after initiation to begin producing tornadoes, while the nontornadic supercell began weakening about two hours into its life. Perhaps the nontornadic supercell merely did not have the opportunity to move into a slightly more favorable environment and/or properly develop storm processes conducive to near-surface rotation as the tornadic supercell did.

On the other hand, Cell A interacted with the northern flank of the tornadic supercell in a seemingly favorable way, as the tornadic supercell then proceeded to produce two tornadoes and survive for 4 additional hours.

The evolution of the two tornadoes and the mesocyclone in the tornadic supercell were also analyzed. During the time period between the two tornadoes, the circulation generally maintained or exceeded tornado strength at most heights, while closer to the surface, the circulation must have weakened, as there was no visible condensation funnel. The same mesocyclone produced both tornadoes, but after the second tornado, interesting cycling of the mesocyclone occurred. Two new midlevel circulations developed in the rear-flank region and moved rearward relatively quickly aloft. An anticyclonic circulation, on the other hand, remained anchored in the hook.

5. Future work

Future work will focus on how interactions with Cell A may have helped the tornadic supercell produce a tornado.

Twenty minutes prior to tornadogenesis, outflow from Cell A had begun interacting with the northern flank of the tornadic supercell (Fig. 11). These interactions may have favorably influenced baroclinicity and/or convergence in the tornadic supercell.

To study this, as well as what could have happened in the nontornadic supercell had it not experienced the detrimental merger, model simulations of this case using data assimilation techniques will be performed.

6. Acknowledgments

References

Barnes, S., 1964: A technique for maximizing details in numerical weather-map analysis. *J. Appl. Meteor.*, **3**, 396–409.

Biggerstaff, M., and Coauthors, 2005: The shared mobile atmospheric research and teaching radar: a collaboration to enhance research and teaching. *Bull. Amer. Meteor. Soc.*, **86**, 1263–1274.

Brandes, E., 1977: Flow in severe thunderstorms observed by dual-doppler radar. *Mon. Wea. Rev.*, **105**, 113–120.

Burgess, D., V. Wood, and R. Brown, 1982: Mesocyclone evolution statistics. Preprints, *12th Conf. on Severe Local Storms*, San Antonio, Texas, Amer. Meteor. Soc., 422-424.

Dowell, D., and H. Bluestein, 2002: The 8 june 1995 mclean, texas, storm. part i: Observations of cyclic tornadogenesis. *Mon. Wea. Rev.*, **130**, 2626–2648.

Dowell, D., and A. Shapiro, 2003: Stability of an iterative dual-doppler wind synthesis in cartesian coordinates. *J. Atmos. Oceanic Technol.*, **20**, 1552–1559.

French, M., H. Bluestein, D. Dowell, L. Wicker, M. Kramar, and A. Pazmany, 2008: High-resolution, mobile doppler radar observations of cyclic mesocyclogenesis in a supercell. *Mon. Wea. Rev.*, **136**, 4997–5016.

Koch, S., M. DesJardins, and P. Kocin, 1983: An interactive barnes objective map analysis scheme for use with satellite and conventional data. *J. Climate Appl. Meteor.*, **22**, 1487–1503.

Majcen, M., P. Markowski, Y. Richardson, D. Dowell, and J. Wurman, 2008: Multipass objective analyses of doppler radar data. *J. Atmos. Oceanic Technol.*, **25**, 1845–1858.

Markowski, P., M. Majcen, Y. Richardson, J. Marquis, and J. Wurman, 2011: Characteristics of the wind field in three nontornadic low-level mesocyclones observed by the doppler on wheels radars. *Electron. J. Severe Storms Meteor.*, **6**, 1–48.

Markowski, P. M., J. M. Straka, and E. N. Rasmussen, 2002: Direct surface thermodynamic observations within the rear-flank downdrafts of nontornadic and tornadic supercells. *Mon. Wea. Rev.*, **130**, 1692–1721.

Oye, R., C. Mueller, and S. Smith, 1995: Software for radar transla-
    tion, visualization, editing, and interpolation. Preprints, *27th Conf.
    on Radar Meteor.*, Vail, CO, Amer. Meteor. Soc., 359-361.

Straka, J. M., E. N. Rasmussen, and S. E. Fredrickson, 1996: A mo-
    bile mesonet for fine-scale meteorological observations. *J. Atmos.
    Oceanic Technol.*, **13**, 921–936.

Waugh, S., and S. E. Fredrickson, 2010: An improved aspirated temper-
    ature system for mobile meteorological observations, especially in
    severe weather. Preprints, *25th Conf. on Severe Local Storms*, Den-
    ver, CO, Amer. Meteor. Soc.

Wurman, J., D. Dowell, Y. Richardson, P. Markowski, E. Rasmussen,
    D. Burgess, L. Wicker, and H. Bluestein, 2012: The second verifi-
    cation of the origins of rotation in tornadoes experiment. *Bull. Amer.
    Meteor. Soc.*, **93**, 1147–1170.

Wurman, J., J. Straka, E. Rasmussen, M. Randall, and A. Zahrai, 1997:
    Design and deployment of a portable, pencil-beam, pulsed, 3-cm
    doppler radar. *J. Atmos. Oceanic Technol.*, **14**, 1502–1512.